Journal of Materials Chemistry C

ROYAL SOCIETY OF CHEMISTRY

PAPER

View Article Online
View Journal | View Issue

Check for updates

Cite this: J. Mater. Chem. C, 2025, 13, 15051

A mechanically robust, high electrically and low thermally conducting silicon oxycarbide ceramic composite by spark plasma sintering†

Abhijit Biswas, ‡*[a] Sudaice Kazibwe,‡[b] Shuo Yang,‡[c] Tymofii S. Pieshkov, ‡[ad] Advaith V. Rau, [ef] Shreyasi Chattopadhyay,[a] Kathy Lu, [e] Ching-Wu Chu, [b] Tobin Filleter,*[c] Liangzi Deng *[b] and Pulickel M. Ajayan*[a]

Silicon oxycarbide (SiOC) ceramics derived from pyrolysis of polymer precursors are important for their aerospace, automotive and electronics applications. Here, we investigate the structural and functional properties of a Si–O–C composite obtained *via* a high-temperature spark plasma sintering process of SiOC powders, derived from the pyrolysis of a polysiloxane polymer. Structural characterization reveals the presence of turbostratic carbon, SiO_2, and SiC domains in the Si–O–C matrix composite. Mechanically, it shows a hardness of ~5.5 GPa and a Young's modulus of ~40 GPa. The composite shows semiconducting behavior at room temperature with electrical conductivities of ~95 S cm^{-1} (in-plane) and ~215 S cm^{-1} (out-of-plane), p-type charges with a carrier density of ~10^{21} cm^{-3} and a mobility of ~0.25 cm^2 V^{-1} s^{-1}, which remains almost temperature independent. The temperature coefficient of resistivity is found to be a very low value of −0.0012 $°C^{-1}$. We also measured a cross-plane thermal conductivity of ~1.14 W m^{-1} K^{-1} at 300 K which exhibits temperature-independent behavior. Our observations are valuable for designing oxycarbide ceramic-based energy efficient devices for advanced applications.

Received 14th February 2025,
Accepted 9th June 2025

DOI: 10.1039/d5tc00653h

rsc.li/materials-c

Open Access Article. Published on 10 June 2025. Downloaded on 5/7/2026 9:46:00 PM.
This article is licensed under a Creative Commons Attribution 3.0 Unported Licence.

1. Introduction

Silicon oxycarbide (Si–O–C) ceramics derived from the pyrolysis of polysiloxanes (silicon-based polymeric precursors) under an inert atmosphere are a unique class of advanced materials that combine the unique properties of silicon, oxygen, and carbon in a single ceramic matrix.[1–3] These composites are known for their exceptional thermal stability, high mechanical strength, and resistance to oxidation, making them ideal for high-performance applications in extreme environments, such as aerospace, energy, and electronics.[4–8] The incorporation of carbon into the silicon-oxide matrix not only enhances the material's toughness and flexibility but also reduces its thermal conductivity, which is beneficial for applications where insulation or heat resistance is required.[9] Si–O–C composites have a unique microstructure that allows for excellent resistance to thermal shock, corrosion, and wear, which is crucial in applications requiring electrical insulation.[10,11] Furthermore, their ability to retain mechanical integrity at elevated temperatures makes Si–O–C composites promising materials for high-temperature structural components, coatings, and thermal protection systems.[12] The synthesis of Si–O–C composites can be achieved through various techniques, *e.g.* polymer precursor chemistry, sol–gel and laser chemical vapor deposition (LCVD) methods, which allow for precise control over the material's composition, microstructure, and properties with the achievement of reasonable functional properties.[13–15]

Recently, an unconventional route of a high-temperature high-pressure (HPHT) spark plasma sintering (SPS) process has emerged as an effective method for producing advanced ceramics, especially those with enhanced mechanical properties and tailored electrical and thermal conductivities.[16,17] SPS,

[a] Department of Materials Science and Nanoengineering, Rice University, Houston, TX, 77005, USA. E-mail: 01abhijit@gmail.com, ajayan@rice.edu
[b] Department of Physics and Texas Center for Superconductivity (TcSUH), University of Houston, Houston, TX, 77004, USA. E-mail: ldeng2@central.uh.edu
[c] Department of Mechanical & Industrial Engineering, University of Toronto, 5 King's College Road, Toronto, M5S 3G8, Canada. E-mail: filleter@mie.utoronto.ca
[d] Applied Physics Graduate Program, Smalley-Curl Institute, Rice University, Houston, TX, 77005, USA
[e] Department of Mechanical and Materials Engineering, University of Alabama at Birmingham, Birmingham, AL 35294, USA
[f] Department of Materials Science and Engineering, Virginia Polytechnic Institute and State University, Blacksburg, VA 24061, USA

† Electronic supplementary information (ESI) available. See DOI: https://doi.org/10.1039/d5tc00653h

‡ Abhijit Biswas, Sudaice Kazibwe, Shuo Yang, and Tymofii S. Pieshkov equally contributed to this work.

Open Access Article. Published on 10 June 2025. Downloaded on 5/7/2026 9:46:00 PM.
This article is licensed under a Creative Commons Attribution 3.0 Unported Licence.

which utilizes pulsed direct current to rapidly heat and consolidate powders under high pressure, allows for the precise control of porosity and grain sizes, leading to composites with exceptional mechanical properties, such as high hardness and stiffness. This unique synthesis technique not only enhances the density and homogeneity of the composites but also ensures that the resulting Si–O–C ceramic materials retain their excellent properties, making them suitable for use in specialized fields where these properties are required.[13,18] Here, we explore the structural, mechanical, electrical and thermal properties of a high-temperature spark plasma sintered Si–O–C ceramic composite from SiOC powders obtained from the pyrolysis of polymeric precursors, polysiloxanes, highlighting its structure–property relationships, and emerging uses in advanced engineering applications.

2. Experimental section

2.1 Spark plasma sintering of SiOC powder

Polysiloxane (PSO, Polyramic® SPR-684 by Starfire Systems, Inc., Schenectady, NY) was used as the precursor material for this study. A Pt catalyst (2% platinum–divinyltetramethyldisiloxane complex in xylene) was procured from Gelest Inc., Morrisville, PA, and was used for crosslinking of PSO. Initially, PSO was blended with 2.5 ppm of the diluted Pt catalyst solution (1 wt% relative to PSO). The homogenized PSO solution was degassed and subjected to cross-linking for 12 hours at 120 °C in an oven. Subsequently, the derived samples underwent pyrolysis in an argon atmosphere at temperatures between 1000 °C and 1400 °C. All pyrolysis experiments were conducted using a horizontal tube furnace (model 1730-20, CM Furnaces Inc., Bloomfield, NJ). The pyrolysis process was carried out at heating and cooling rates of 2 °C minute^{-1} and soaking at the peak temperature for 2 hours.

The SPS was performed using an SPS 25-10 machine (Thermal Technology LLC, California, USA) at a constant uniaxial pressing pressure of 90 MPa and a heating rate of 50 °C min^{-1}, at the SPS facility at Texas A&M University, USA. The maximum temperature reached was 1800 °C. The sintering process followed this procedure: several grams of powder were placed into a graphite mold (one-inch diameter) and positioned in a sintering chamber under an initial pressure of 5 MPa. It was maintained at approximately 2×10^{-5} Torr for around 30 minutes, then sintered for 60 minutes under atmospheric pressure in an ultra-high purity (5N, ~99.999%) Argon gas atmosphere. The graphite foils are used to wrap the SiOC powder and placed inside the graphite die. Graphite foil also acts as a barrier to prevent unwanted chemical reactions between the sample and the tooling during the sintering process. During the process dc current passes through the material directly which causes the temperature rise because of the Joule heating. Graphite foil helps to trap the temperature inside, improve the heat distribution within the sample and control the temperature with more accuracy. The SPS temperature was monitored using an optical pyrometer (Raytek, Berlin, Germany, model D-13127). After sintering, the pressure was gradually released at ~5 MPa min^{-1}, while the temperature was reduced at approximately 100 °C min^{-1}.

2.2 Spectroscopic, chemical, and microscopic characterization (XRD, XPS, FESEM, FTIR, Raman spectroscopy, DSC-TGA, and HRTEM)

X-ray diffraction (XRD) was conducted using a Rigaku SmartLab thin-film X-ray diffractometer (Tokyo, Japan), operating at 40 kV and 40 mA, with a monochromatic Cu Kα radiation source (λ = 1.5406 Å) at a scan rate of 1° min^{-1}. XPS analysis was performed with a PHI Quantera SXM scanning X-ray microprobe, utilizing a monochromatic Al Kα X-ray source (1486.6 eV). High-resolution core-level scans for B1s and N1s were recorded at a pass energy of 26 eV. FTIR spectra were acquired using a Nicolet 380 FTIR spectrometer with a single-crystal diamond window. Raman spectroscopy measurements were carried out with a Renishaw inVia confocal microscope, using a 532 nm laser as the excitation source. Surface topography was examined using field emission scanning electron microscopy (FESEM) (FEI Quanta 400 ESEM FEG).

Simultaneous thermal analysis ((DSC-TGA; DSC (differential scanning calorimetry) and TGA (thermogravimetric analysis)) were performed using a TA Instruments SDT 650 analyzer (New Haven, CT, USA) with a heating rate of 5 °C min^{-1} and an Ar flow rate of 20 mL min^{-1} from room temperature to 1500 °C, and calibrated with a sapphire standard.

The HRTEM images were obtained *via* aberration corrected Titan Themis^3 (S)TEM at 300 kV accelerating voltage. We coated chromium and platinum on the surface. HRTEM images were smoothed using ImageJ software with a low pass filter, cutting out the higher frequencies in the fast Fourier transformation. The camera length in the diffraction patterns was 360 and 460 mm. We additionally applied high-pass and radial Wiener filters to the image to distinguish the regions.

2.3 Nanoindentation characterization

Nanoindentation measurements were conducted at six locations across the sample using a Berkovich diamond indenter (KLA Instruments, iMicro) with 0.15 N force to ensure reliable results. The nanoindentation system was calibrated using a standard fused silica specimen before each experiment. A system strain rate of 0.2 s^{-1} was applied, with a hold time of 1.0 s at maximum load. The target drift rate was maintained at 0.1 nm s^{-1}, and testing commenced only when the sample drift was below this threshold. Hardness and modulus values were determined using the Oliver and Pharr method from Load-displacement data.

2.4 Resistivity and the Hall effect

Using the physical property measurement system (PPMS) from quantum design, we measured the DC resistivity of a rectangular Si–O–C sample as a function of temperature, ranging from 2 to 300 K, at a rate of 1 K min^{-1}. For the measurements, a constant current of 5 mA was applied along the *ab*-plane (in-plane), or the *c*-axis (out-of-plane) and the voltage was measured. The measurements were performed using the standard

 This journal is © The Royal Society of Chemistry 2025

Open Access Article. Published on 10 June 2025. Downloaded on 5/7/2026 9:46:00 PM. This article is licensed under a Creative Commons Attribution 3.0 Unported Licence.

four-point probe method with silver point contacts. Hall resistivity data were collected at a magnetic field of 6 T (applied parallel to the *c*-axis of the 465 μm thick SiOC sample) and an excitation current of 10 mA, using the AC transport option of the quantum design PPMS in a van der Pauw geometry with four symmetrically placed contacts to ensure isotropic current flow. The polarity of the magnetic field was systematically reversed to eliminate any magnetoresistive components caused by misalignment of the voltage contacts.

2.5 Thermal conductivity

The cross-plane thermal conductivity ($\kappa_\perp$) of silicon oxycarbide (Si–O–C) samples with a diameter of 0.5 inch (12.7 mm) and a thickness of 2 mm was measured across a temperature range of 50–600 °C using a laser-flash thermal diffusivity testing machine (DLF-1200 laser flash) in an inert nitrogen environment. This method involves determining thermal diffusivity, which represents a material's ability to transfer heat through its structure. The process begins by applying a short pulse of heat energy to one surface of the sample. The temperature response on the opposite side is then recorded over time to create a thermogram. The thermogram provides critical information about thermal diffusivity (a), along with the specific heat capacity (C_p) from the DSC data, and density (ρ) of the material is used to compute the thermal conductivity (k) using the formula $k = a \times C_p \times \rho$.

3. Results and discussion

3.1 Structural, chemical and microscopic characterization

First, we investigated the stability of SiOC precursor powder obtained from the pyrolysis process. We performed the temperature dependent XRD in the oxidative environment of the as-prepared SiOC powder. Till 500 °C, SiOC remains stable in air, however, above this temperature carbon possibly evaporates and the black powder turns white with the appearance of SiO_2 and SiC peaks (Fig. S1, ESI†). As reported in the literature, SiOC is stable up to 1000 °C in air and known for its thermal stability in inert atmospheres at much higher temperature.[19] Therefore, we prepared a Si–O–C ceramic disk by using the high-temperature SPS process at 1800 °C and 90 MPa for 1 h (Fig. 1a), under an ultra-high purity (~99.999%) argon gas atmosphere. By using the solid cylinder formula the density of the disk was measured to be ~1.67 g cm^{-3} (whereas the theoretical density of SiOC is ~2.4 g cm^{-3}).[19,20] Using the formula porosity = 1 − (apparent density/real density),[20] the porosity is calculated to be ~30.5%. First, we performed FESEM and energy dispersive X-ray spectroscopy (EDS) mapping showing the overall features of the granular top surface and the presence of Si, O and C in the sample (Fig. 1b and e). The XRD of SPS Si–O–C shows the presence of crystalline SiO_2 (cristobalite phase), graphitic carbon (Card No. 00-041-1487) and β-SiC (Card No. 00-029-1129) phase related peaks (Fig. 1f).[9,12,21] By fitting the broad carbon peak, we extracted the free C percentage of ~45.35% (Fig. S2, ESI†). The Raman spectra show the presence of a disordered D-band (~1340.7 cm^{-1}) attributed to disorder-induced vibrational mode of nano-crystalline graphitic (or graphene-like) species with domain boundaries as well as graphitic G-bands (~1588.1 cm^{-1}), attributed to in-plane vibrational motion of the carbon–carbon sp^2-bond structure, respectively (Fig. 1g).[22,23] The ratio of D-band and G-band intensity (I_D/I_G) is ~1.61, indicative of the crystallinity of the graphitic clusters.[14] A small hump around 1102 cm^{-1} originated from SiO_2. Fourier transform infrared spectroscopy (FTIR) shows the peaks related to Si–Si (558.3 cm^{-1}), Si–C (875.9 cm^{-1}), Si–O–Si (1069.1 cm^{-1}), Si–O (1258.6 cm^{-1}), and C=C (1418.3 cm^{-1}) (Fig. 1h).[18] We performed the XPS elemental scans of Si 2p, O 1s and C 1s edges, which further show the presence of all these Si/O/C bonding related peaks (Fig. 1i–k).[15,24–26] The obtained wt% values from the elemental scans are Si : O : C 13.91 : 18.29 : 67.79. We also extracted at% of all the bonded peaks from XPS (Table 1).

We performed the DSC-TGA test of both SiOC powder obtained from pyrolysis of a preceramic polysiloxane and the SPS Si–O–C ceramic. Both the as-prepared SiOC powder and SPS Si–O–C exhibited no mass loss (Fig. S3a, ESI†) up to 700–800 °C. In SPS Si–O–C, gradual gas evolution (*e.g.*, CO, H_2) contributed to ~7–8% mass loss between 700 °C and 1400 °C prior to a substantial 4% decrease up to 1500 °C, the latter is from carbothermal reduction of SiO_2 domains to form β-SiC. However, the as-prepared SiOC precursor did not experience gas volatilization until 1300 °C, with a similar yet less pronounced carbothermal reduction event between 1400 °C and 1500 °C. Due to improved diffusion of C in the SiO_2 domains from SPS (as shown in Fig. S3b, ESI†), the carbothermal reaction rate was enhanced in SPS Si–O–C compared to as-prepared SiOC. Notably, both as-prepared SiOC and SPS Si–O–C experienced similar internal kinetic events at ~500 °C and ~625 °C (minor) that were not correlated with any mass loss events (Fig. S3b, ESI†). This phenomenon was attributed to internal bond rearrangements among Si tetrahedra in the amorphous SiOC matrix, indicating that there was some recrystallization behavior intrinsic to SiOC that was not appreciably inhibited after the SPS process. As such, both as-prepared SiOC and SPS Si–O–C were deemed to be thermally stable below 500 °C in terms of both mass loss and internal kinetic events as the SPS process did not suppress recrystallization inherent to this material. As carbothermal reduction was only expected above 1300 °C, mass loss in SPS Si–O–C between 700 °C and 1400 °C was postulated to occur from CO or H_2 gas release due to the effects of C ingress within SiO_2 domains from SPS and intrinsic bond restructuring between 500 °C and 600 °C.

To gain insights into the microstructure of the SPS Si–O–C composite, we performed cross-sectional high-resolution transmission electron microscopy (HRTEM) of the sample. As shown in the HRTEM image, the sample shows the presence of grains and grain boundaries. The grain sizes are in the 100–500 nm range (vertically), whereas they exceed 1000 nm in the horizontal direction (Fig. 2a). The colored EDAX map shows that the grain consists of SiO_2 (green), C (red) and SiC (mixed green/red) (Fig. 2b). The SiC region shows a poorly aligned arrangement of graphitic sheets (''rippled'' or ''wrinkled'' like) with an

Open Access Article. Published on 10 June 2025. Downloaded on 5/7/2026 9:46:00 PM.
This article is licensed under a Creative Commons Attribution 3.0 Unported Licence.

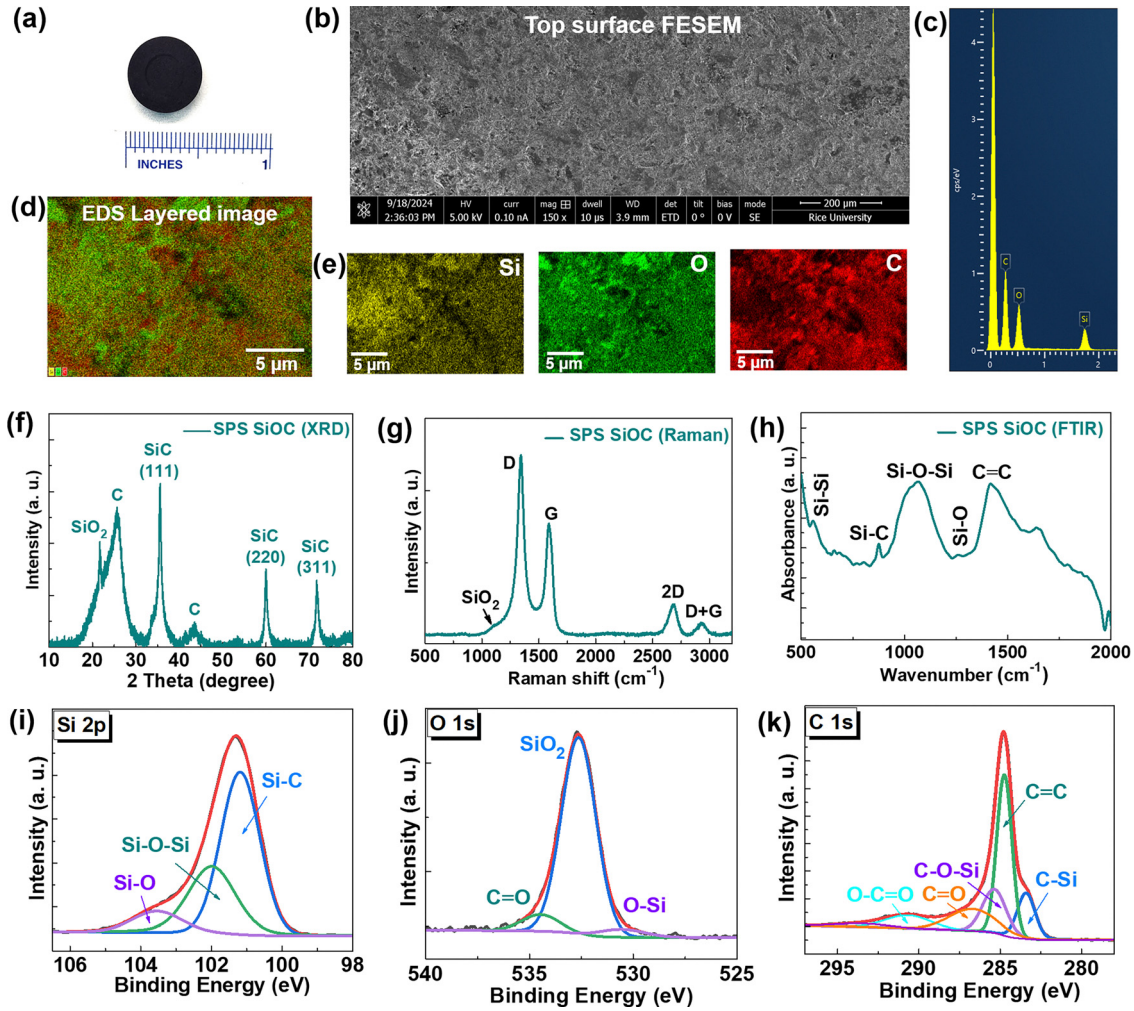

Fig. 1 Structural characterization of the SPS Si–O–C disk. (a) A spark plasma sintered (1800 °C and 90 MPa pressure for one hour) compact high-density disk of SiOC. (b) Top-view FESEM showing the overall features of the surface. (c)–(e) EDS mapping, layered elemental image, and elemental mapping showing the distribution of Si, O and C. (f) XRD shows the diffraction peaks related to the cristobalite phase SiO_2, β-SiC and C. (g) Raman spectra showing the D and G-bands corresponding to disordered and graphitic carbon. (h) FTIR spectra showing the several bonding features related to Si–O–C. (i)–(k) Core-level XPS elemental scans of Si 2p, O 1s and C 1s peaks also show several bonding features related to Si–O–C.

Table 1 Atomic percentage of peaks obtained from the XPS peak fitting

Core level	Peak	Binding energy (eV)	At (%)
Si 2p	Si–C	101.19	64.47
	Si–O–Si	101.98	28.71
	Si–O	103.47	6.82
O 1s	O–Si	530.37	2.83
	Si–O–Si (SiO_2)	532.62	88.60
	C═O	534.36	8.57
C 1s	C–Si	283.39	14.98
	C═C	284.75	44.11
	C–O–Si	285.38	20.34
	C═O	287.02	12.10
	O–C═O	290.48	6.89
	Π–Π*	292.14	1.57

interlayer *d*-spacing of ∼0.35 nm and some regions of nanocrystalline SiC particles (Fig. 2c). This behavior seems typical for all SiC regions across the sample, while pure carbon regions closer to SiO_2, have an amorphous structure (Fig. 2d). We also provide additional images with higher magnification and better resolution with several SiC particles present. These images clearly represent the nanocrystalline SiC particles with an interplanar *d*-spacing of 0.25 nm, corresponding to the (111) plane of β-SiC (Fig. S4a, ESI†). For clarity purposes, we additionally applied high-pass and radial Wiener filters to the image to distinguish the SiC lattice from the carbon background (Fig. S4b, ESI†). Polycrystalline nature of β-SiC found from the electron diffraction analysis (Fig. 2e) can be explained by the presence of nanocrystalline particles ∼12–25 nm in diameter that are present throughout this area, blending with amorphous and turbostratic carbon. Although the SiO_2 region also shows an amorphous structure (Fig. 2f), similar to the C region, in all three diffraction patterns we can see the same first ring from the SiC. Additionally, SiO_2 electron diffraction shows several spots from second and third polycrystalline rings of SiC,

 This journal is © The Royal Society of Chemistry 2025

Open Access Article. Published on 10 June 2025. Downloaded on 5/7/2026 9:46:00 PM.
This article is licensed under a Creative Commons Attribution 3.0 Unported Licence.

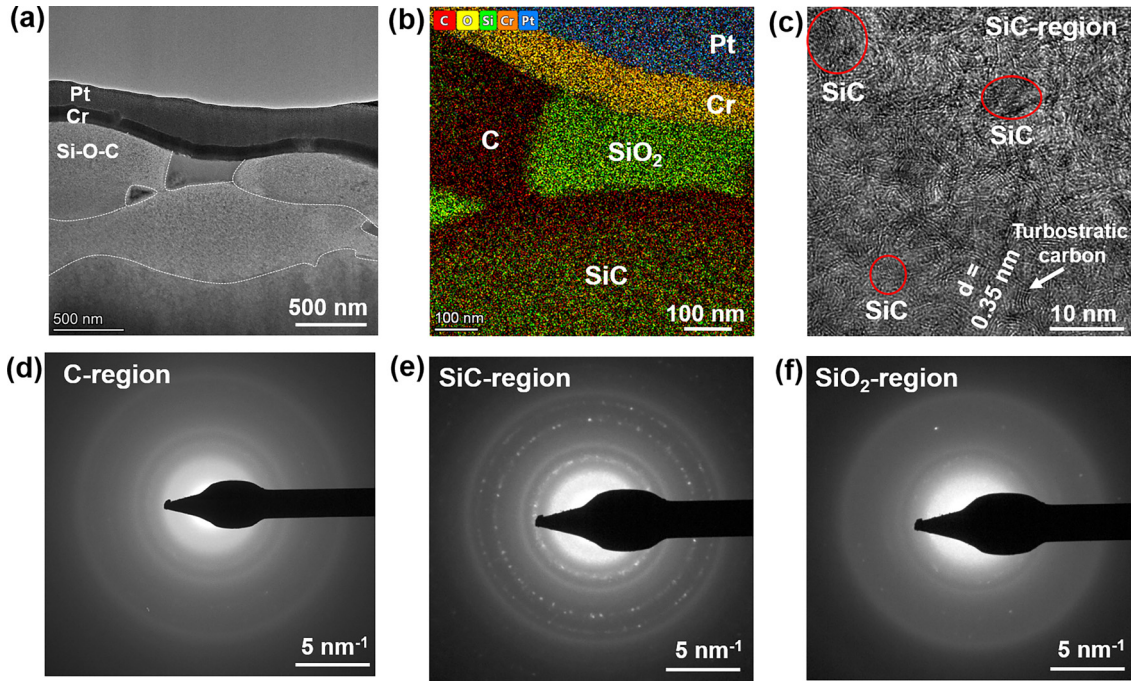

Fig. 2 Cross-sectional high-resolution transmission electron microscopy (HRTEM). (a) Cross-sectional HRTEM image showing the Si–O–C composite layer, conducting chromium and protecting the Pt layer. The white dotted lines correspond to the grain boundaries. (b) Colored elemental map of the zoomed region showing the presence of C, SiC and SiO_2 grains in the Si–O–C matrix. (c) In the SiC region, separate SiC particles are seen (red circles) as well as layer fringes with a d-spacing of $\sim$0.35 nm, related to turbostratic carbon. (d)–(f) Diffraction patterns at different regions (C, SiC and SiO_2) confirm the overall amorphous nature with the presence of some polycrystalline regions.

possibly occurring because there are additional isolated SiC particles inside respective regions.

3.2 Mechanical characterization

We measured the mechanical strength of the SPS Si–O–C ceramics by using the nanoindentation method. It was performed at six different regions of the sample to confirm the homogeneity. The mechanical properties depend on the porosity, composition, structure and crystallization depending on the SPS sintering temperature.[27] As is shown, at every place the sample almost shows a similar feature in the load *vs.* displacement curve (Fig. 3a). The inset shows the atomic force microscopy (AFM) micrographs of the Berkovich indent. The measured hardness (H_v) and Young's modulus of the sample were 5.5 $\pm$ 1.1 GPa and 40.3 $\pm$ 3.4 GPa (Fig. 3b). In the literature, it has been shown that as the amount of carbon increased, the H_v of SPS Si–O–C derived materials decreased from 9.2 to 5.4 GPa, which is almost similar to our observations.[11,13,27]

3.3 Electrical and thermal characterization

The electrical conductivity (σ) of SPS Si–O–C shows semi-conducting-like behavior with an in-plane conductivity (σ_{ab}) of

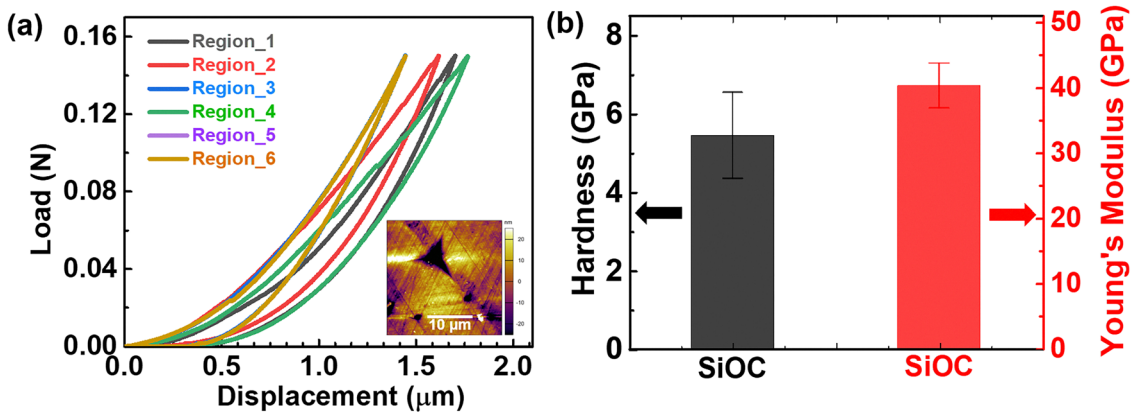

Fig. 3 Mechanical properties of the SPS Si–O–C disk. (a) The load–displacement curves obtained during the nanoindentation process at several points of the sample. Inset shows the AFM images across the depth of the indent. (b) The measured hardness and Young's modulus of Si–O–C.

Open Access Article. Published on 10 June 2025. Downloaded on 5/7/2026 9:46:00 PM.
This article is licensed under a Creative Commons Attribution 3.0 Unported Licence.

$\sim$95 S cm^{-1} and an out-of-plane conductivity (σ_c) of $\sim$215 S cm^{-1} at room temperature, showing a negligible increase down to low temperature (Fig. 4a). In the literature, the best σ value reported for the Si–O–C ceramic (sintered at 1650 °C by a conventional ceramic processing route) is $\sim$7 S cm^{-1} at room temperature.[28] Our sample shows more than one order higher σ value possibly due to better compactness and less porosity produced by the high temperature (1800 °C) SPS process which results in C inducing shallow impurity levels in SiC, leading to a lower activation energy (E_a $\sim$44 meV; Fig. S5, ESI†) and a higher σ value than reported values.[19,22,26] To investigate the possibility of the texture effect which might cause anisotropic nature, we also performed the in-plane XRD of the SPS Si–O–C disk (Fig. S6, ESI†). In both the directions it shows the presence of all the peaks. In-plane XRD shows lower intensity (causing less pronounced diffraction patterns) because it measures diffraction from planes parallel to the sample surface. Thus, it is difficult to differentiate the preferred orientation just based only on intensity counts. However, it does appear like there is a slightly higher concentration of surface SiO_2 compared to SiC in the in-plane *versus* out-of-plane, which would most likely account for the anisotropy because there is some passivating SiO_2 layer. The in-plane probably sees more SiO_2 than SiC or C, so has lower conductivity, while those surface effects are minimized with the out-of-plane measurement. Moreover, the changes in σ with temperature remains low (σ_{ab} $\sim$ 70 S cm^{-1} and σ_c $\sim$ 152 S cm^{-1} at 2 K). The temperature coefficient of resistivity (TCR) value is found to be low of -0.0012 °C^{-1}. Typically, amorphous C shows a TCR value of -0.0005 ppm °C^{-1}. Hall effect measurements show the p-type (hole) charge carriers (inset of Fig. 4b shows the negative slope in Hall voltage) with a carrier density of $\sim 10^{21}$ cm^{-3} (Fig. 4b), consistent with the previous results.[23] The p-type charge carriers of Si–O–C are attributed to the high electrical conductivity of the sp^2-bond clusters.[23] The hole mobility (μ) was found to be low of $\sim$0.2 cm^2 V^{-1} s^{-1} which almost remains temperature independent. Low TCR and almost temperature-independent mobility are significant because they ensure that the hole conduction properties of semiconductor materials remain stable across a range of temperatures.

We also measured the thermal diffusivity and specific heat capacity (C_p), and consequent cross-plane thermal conductivity ($\kappa_\perp$) value of the sample was found to be 1.14 W m^{-1} K^{-1} at room temperature (Fig. 4c and d). In principle, $\kappa_\perp$ values depend on porosity, defects in grain boundaries, the degree of crystallinity, the size of crystallites and the presence of different phases. We also investigated the temperature dependence of $\kappa_\perp$ of the sample finding that it shows almost temperature-independent feature. SPS Si–O–C consists of the

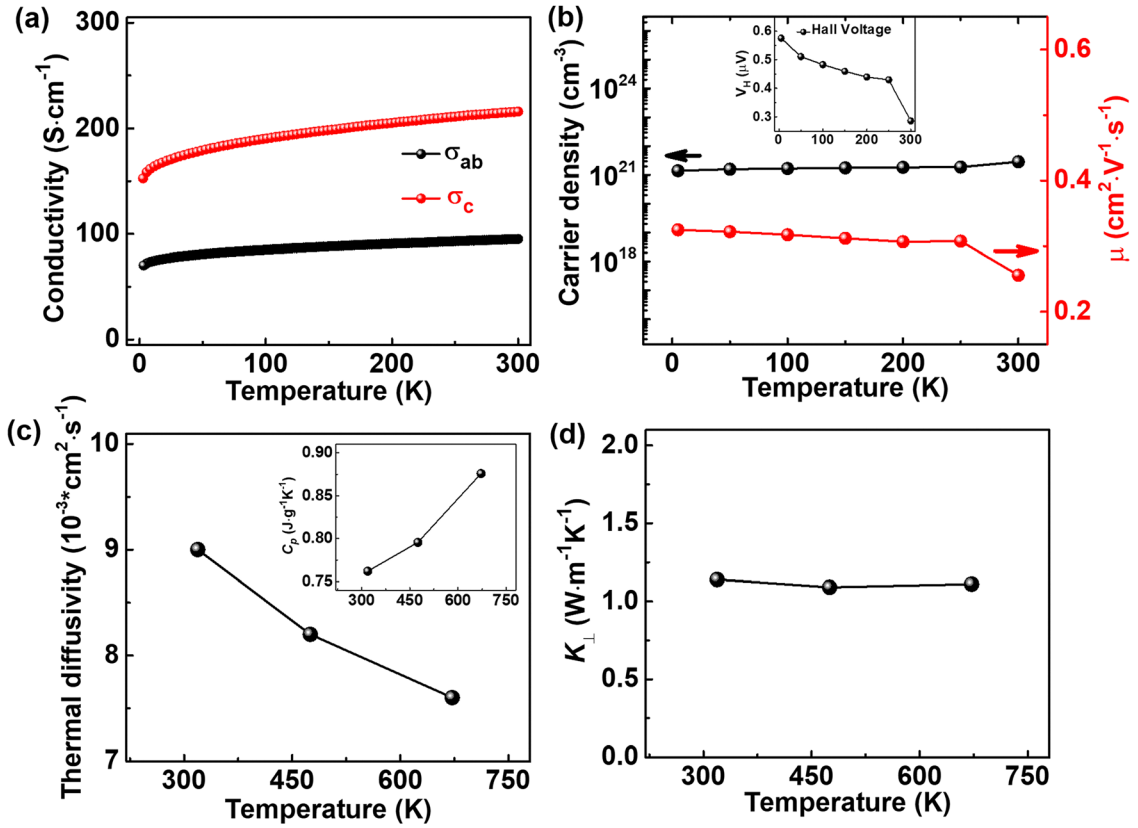

Fig. 4 Electrical and thermal conductivity of the SPS Si–O–C sample. (a) Temperature dependent anisotropic electrical conductivity showing a slight decrease even at low temperature confirming the semiconducting behavior. (b) Hall effect measurement showing the temperature dependent carrier density and mobility. Inset shows the measured hall voltage (V_H) determining the carrier type. Temperature dependent (c) thermal diffusivity, specific heat capacity (inset) and (d) thermal conductivity which remains nearly temperature independent.

 This journal is © The Royal Society of Chemistry 2025

Open Access Article. Published on 10 June 2025. Downloaded on 5/7/2026 9:46:00 PM. This article is licensed under a Creative Commons Attribution 3.0 Unported Licence.

Table 2 Room temperature properties of Si–O–C ceramics prepared by various methods

Sintering conditions	Hardness (GPa)	Young's modulus (GPa)	Electrical conductivity (S cm^{-1})	Thermal conductivity (W m^{-1} K^{-1})	Ref.
1800 °C, 90 MPa (SPS)	5.5	40	95 (in-plane) 215 (out-of-plane)	1.14	This work
1300–1500 °C (SPS)	3.4–9.15			1.38	13
1300–1700 °C, (SPS)			0.001	1.4–1.83	22
1550 °C, 40 MPa (hot pressing)			22.2		23
1100 °C (warm pressing)	6.4	101			27
1450–1650 °C (conventional)			1–7		28
1300–1700 °C, 40 MPa (SPS)	12	95			20
1400–1600 °C (hot pressing)	7.2				30
1600 °C (SPS)				2.15–2.7	31
1600 °C (hot pressing)				1.5–1.8	32

Si–O–C matrix that is irregularly distributed within SiC and graphite nanodomains.[29] This possibly prevents the crystallization of the silica matrix, and promotes trivial crystallization of both the silicon carbide and graphite phases.[20,26] Therefore, the intrinsic microstructure of Si–O–C plays a crucial role in phonon transport, as the interfaces between SiO_2, SiC and graphite induced phonon-scattering and reduced the thermal conductivity.[30–32]

The above results obtained for the SPS Si–O–C ceramic composite show various interesting functional properties. Table 2 presents a summary of the mechanical, electrical, and thermal properties of the SPS Si–O–C composite as well as their comparison with the existing literature. Structurally, the material contains SiO_2, β-SiC, and C grains. XRD and XPS analyses indicate that the C phase comprises ~55% ordered C and ~45% free C. In addition, the SPS Si–O–C disk shows ~30.5% porosity. Regarding the functional properties, generally mechanical hardness is affected by the material's porosity and C content. The measured hardness of 5.5 GPa is comparable to that of silica glass (6–7 GPa), suggesting that the hardness is primarily influenced by the presence of silica grains.[13] The composite exhibits high anisotropic electrical conductivity that remains nearly constant with temperature. This behavior is due to charge carrier percolating through ordered sp^2 graphitic domains within the C grains, in addition to some contributions from the nanocrystalline β-SiC phase.[23,28] In view of cross-plane thermal conductivity (κ), the SPS Si–O–C material shows a relatively low value of 1.14 W m^{-1} K^{-1} at room temperature, which is comparable to those of silica glass (~1.44 W m^{-1} K^{-1}) and bulk porous SiC (~2 W m^{-1} K^{-1}), but significantly lower than those of fully dense ordered SiC (~169–206 W m^{-1} K^{-1}) and graphite (~600 W m^{-1} K^{-1}).[13,32] This thermal behavior can be related to the microstructural features, particularly to the turbostratic nature of C, silica and β-SiC. At lower temperatures nanoparticle scattering and interface scattering can dominate thermal conductivity, especially in nanostructured or composite materials. Also, phonon–phonon scattering is greatly reduced at low temperatures due to the low phonon population. Several reports showed that the κ of Si–O–C is nearly independent of porosity and temperature.[13,31,32] We also obtained almost temperature independent κ-values with increasing temperature up to 680 K, consistent with the disordered or amorphous solids.[31,32] Overall, the mechanical and thermal properties of the SPS Si–O–C ceramic composite were governed by SiO_2 and β-SiC, but the electrical properties were the result of the C phases within the composite.

4. Conclusion

In summary, we produced a high-density Si–O–C ceramic composite through a high-temperature spark plasma sintering process, using SiOC powder derived from the pyrolysis of a polysiloxane polymer precursor under an inert atmosphere. The obtained high density composite ceramic exhibited excellent mechanical hardness and stiffness and high electrical and low thermal conductivity, which could pave the way for novel applications (*e.g.* protective coating materials, electronics, thermal sensing and thermal managements) of silicon oxycarbide based materials.

Author contributions

A. B. and P. M. A. conceptualized the study. A. B., T. P. and S. C. performed the characterization. S. K., C. C. and L. D. performed the electrical measurements. S. Y. and T. F. performed the nano-indentation and thermal conductivity characterization. A. V. R. and K. L. provided the powder sample and the DSC-TGA data. All the authors discussed the results and contributed to the manuscript preparation.

Conflicts of interest

The authors declare that they have no known competing financial interests or personal relationships that could have appeared to influence the work reported in this paper.

Data avialibiity

The data that support the findings of this study are available from the corresponding author upon reasonable request.

Open Access Article. Published on 10 June 2025. Downloaded on 5/7/2026 9:46:00 PM.
This article is licensed under a Creative Commons Attribution 3.0 Unported Licence.

Acknowledgements

This work was sponsored by the Department of the Navy, Office of Naval Research under Award Number 000541684-SC001. This material is based upon work supported by Air Force Office of Scientific Research under Award Number FA9550-24-1-0301, U.S. Air Force Office of Scientific Research Grants FA9550-15-1-0236 and FA9550-20-1-0068; the T. L. L. Temple Foundation; the John J and Rebecca Moores Endowment; and the State of Texas through the Texas Center for Superconductivity at the University of Houston. L. Z. D. is supported by the Robert A. Welch Foundation (00730-5021-H0452-B0001-G0512489) T. F. acknowledges financial support from the Natural Sciences and Engineering Research Council of Canada (NSERC) and the Canada Foundation for Innovation (CFI). A. B. would like to thank Texas A&M for the SPS process.

References

1 C. Stabler, E. Ionescu, M. Graczyk-Zajac, I. Gonzalo-Juan and R. Riedel, *J. Am. Ceram. Soc.*, 2018, **101**, 4817–4856.
2 E. Barrios and L. Zhai, *Mol. Syst. Des. Eng.*, 2020, **5**, 1606–1641.
3 G. Mera, A. Navrotsky, S. Sen, H.-J. Kleebe and R. Riedel, *J. Mater. Chem. A*, 2013, **1**, 3826–3836.
4 R. Bura, B. Kumar and R. M. Prasad, *Int. J. Appl. Ceram. Technol.*, 2024, **21**, 900–909.
5 R. Sujith, J. Gangadhar, M. Greenough, R. K. Bordia and D. K. Panda, *J. Mater. Chem. A*, 2023, **11**, 20324–20348.
6 J. D. Torrey, R. K. Bordia, C. H. Henager, Y. Blum, Y. Shin and W. D. Samuels, *J. Mater. Sci.*, 2006, **41**, 4617–4622.
7 F. Kolář, V. Machovič, J. Svítilová and L. Borecká, *Mater. Chem. Phys.*, 2004, **86**, 88–98.
8 Y. Jia, T. D. Ajayi, M. A. J. Roberts, C.-C. Chung and C. Xu, *ACS Appl. Mater. Interfaces*, 2020, **12**, 46254–46266.
9 J. Li, K. Lu, T. Lin and F. Shen, *J. Am. Ceram. Soc.*, 2015, **98**, 1753–1761.
10 F. Guo, D. Su, Y. Liu, J. Wang, X. Yan, J. Chen and S. Chen, *Ceram. Int.*, 2018, **44**, 13444–13448.
11 M. A. Mazo, A. Tamayo and J. Rubio, *J. Eur. Ceram. Soc.*, 2016, **36**, 2443–2452.
12 K. Lu and D. Erb, *Int. Mater. Rev.*, 2018, **63**, 139–161.
13 M. A. Mazo, C. Palencia, A. Nistal, F. Rubio, J. Rubio and J. L. Oteo, *J. Eur. Ceram. Soc.*, 2012, **32**, 3369–3378.
14 C. Liu, X. Meng, X. Zhang, C. Hong, J. Han, W. Han, B. Xu, S. Dong and S. Du, *Ceram. Int.*, 2015, **41**, 11091–11096.
15 S. Yu, R. Tu and T. Goto, *J. Eur. Ceram. Soc.*, 2016, **36**, 403–409.
16 Z. A. Munir, U. Anselmi-Tamburini and M. Ohyanagi, *J. Mater. Sci.*, 2006, **41**, 763–777.
17 D. B. Kumar, B. S. babu, K. M. A. Jerrin, N. Joseph and A. Jiss, *IOP Conf. Ser.: Mater. Sci. Eng.*, 2020, **993**, 012004.
18 A. Tamayo, M. A. Mazo, F. Rubio and J. Rubio, *Ceram. Int.*, 2014, **40**, 11351–11358.
19 K. Lu, D. Erb and M. Liu, *J. Mater. Chem. C*, 2016, **4**, 1829–1837.
20 M. A. Mazo, D. Soriano and J. Rubio, *Ceram. Int.*, 2023, **49**, 12866–12875.
21 D. Erb and K. Lu, *J. Eur. Ceram. Soc.*, 2017, **37**, 4547–4557.
22 M. A. Mazo, A. Tamayo, A. C. Caballero and J. Rubio, *J. Eur. Ceram. Soc.*, 2017, **37**, 2011–2020.
23 K. J. Kim, J.-H. Eom, T. Y. Koh, Y.-W. Kim and W.-S. Seo, *J. Eur. Ceram. Soc.*, 2016, **36**, 2705–2711.
24 G. Jella, D. K. Panda, N. Sapkota, M. Greenough, S. P. Datta, A. M. Rao, R. Sujith and R. K. Bordia, *ACS Appl. Mater. Interfaces*, 2023, **15**, 30039–30051.
25 G. D. Sorarù, G. D'Andrea and A. Glisenti, *Mater. Lett.*, 1996, **27**, 1–5.
26 J. Gangadhar, A. Maheshwari, R. K. Bordia, C. N. Shyam Kumar, C. Kubel and R. Sujith, *Ceram. Int.*, 2020, **46**, 28156–28164.
27 C. Moysan, R. Riedel, R. Harshe, T. Rouxel and F. Augereau, *J. Eur. Ceram. Soc.*, 2007, **27**, 397–403.
28 K. J. Kim, J.-H. Eom, Y.-W. Kim and W.-S. Seo, *J. Eur. Ceram. Soc.*, 2015, **35**, 1355–1360.
29 Q. Wei, E. Pippel, J. Woltersdorf, M. Scheffler and P. Greil, *Mater. Chem. Phys.*, 2002, **73**, 281–289.
30 M. Esfehanian, R. Oberacker, T. Fett and M. J. Hoffmann, *J. Am. Ceram. Soc.*, 2008, **91**, 3803–3805.
31 C. Stabler, A. Reitz, P. Stein, B. Albert, R. Riedel and E. Ionescu, *Materials*, 2018, **11**, 279.
32 A. Gurlo, E. Ionescu, R. Riedel and D. R. Clarke, *J. Am. Ceram. Soc.*, 2016, **99**, 281–285.

This journal is © The Royal Society of Chemistry 2025